Manufacturing Rev. **11**, 2 (2024)

https://doi.org/10.1051/mfreview/2024001

Manufacturing Review
Available online at:
https://mfr.edp-open.org

RESEARCH ARTICLE OPEN ACCESS

Effects of scanning methods on cracking, microstructures and microhardness of Inconel 625 parts formed by direct laser metal deposition

Tat Doan Khoa[1,*], Van Thao Le[2], Van Nguy Duong[1], and Van Chau Tran[2]

[1] Faculty of Mechanical Engineering, Le Quy Don Technical University, Hanoi, Vietnam
[2] Advanced Technology Center, Le Quy Don Technical University, Hanoi, Vietnam

Received: 25 September 2023 / Accepted: 4 January 2024

Abstract. This study aims at investigating the effects of scanning methods on the stress distribution and microstructures of Inconel 625 thin-walled part fabricated by direct laser metal deposition. The results showed that with the single direction scanning (SDS) method, the residual stress at both the ends of the thin wall was relatively high while the stress at the middle was smaller with a stress difference of about 1800 MPa. In contrast, with the reverse direction scanning (RDS) method, the residual stress in the thin wall was distributed relatively evenly, with a stress difference of about 350 MPa between both the ends and the center. The experimental results showed that, in the SDS method, cracks occurred at both ends and in the middle of the thin wall, whereas in the RDS method, warping and cracks phenomena were eliminated. The microstructure of the Inconel 625 in the forming layer is characterized by a columnar crystal structure that has a small length and grows perpendicularly to the scanning direction. This growth is continuous between the forming layers. In both cases, the microhardness increases with the height of the formed layers. The microhardness values are relatively uniform with values ranging from 420 to 450 HV.

Keywords: Direct laser metal deposition / scanning method / Inconel 625 / residual stress / crack / microstructure

1 Introduction

Inconel 625, a nickel-based superalloy, is the main material for forming aircraft engine parts such as turbine blades and stiffeners. They are difficult to fabricate using traditional casting and forging methods. Therefore, the use of direct laser metal deposition (DLMD) to form thin-walled Inconel 625 components will have a significant impact on the development of the aviation and aerospace industry [1–3]. However, the melting points of each element of Inconel 625 are significantly different. During the forming process, the local part of the component is rapidly heated and then cooled, which cannot make the composition diffuse uniformly. As a result, the chemical composition inside each grain is uneven, resulting in significant stress concentration. Under the thermal stress generated during the solidification process, cracks occur and propagate at the grain boundaries. Cracking of the cladding layer directly affects the quality of the component [4].

In previous research on DLMD, various methods have been used to solve the component cracking during forming. The primary methods include adjusting the material composition to increase plasticity [5], optimizing the process parameters [6], utilizing multiple process composite manufacturing [7], preheating the substrate [8], post-forming heat treatment, and reducing the oxygen content in the protective atmosphere [9]. Although these studies have been effective in reducing cracking during DLMD, there are few publications detailing the stress distribution, crack morphology, and crack distribution of Inconel 625 components formed by DLMD.

This paper aims to study the impact of different scanning modes (i.e., single and reverse scanning directions) on the stress distribution and crack morphology of thin-walled components and simulate the effect of various scanning methods on the stress distribution of Inconel 625 thin-walled components formed by DLMD through numerical simulations. The experiments were also performed to observe the cracking phenomenon, microstructures, and microhardness of thin-walled parts under different scanning methods.

* e-mail: khoadt@lqdtu.edu.vn

Table 1. Composition of Inconel 625 powder.

Element	Ni	Cr	Fe	Mo	Nb + Ta	C	Mn	Si	P	S	Al	Ti	Co
wt.%	>58	20–23	<5	8–10	3.15–4.15	<0.1	<0.5	<0.5	<0.015	<0.015	<0.4	<0.4	<1

Table 2. Composition of 316L substrate.

Element	C	Cr	Ni	Si	Mn	Mo	P	S	Fe
wt.%	0.024	16.75	10.17	0.51	1.53	2.05	0.024	0.003	Bal.

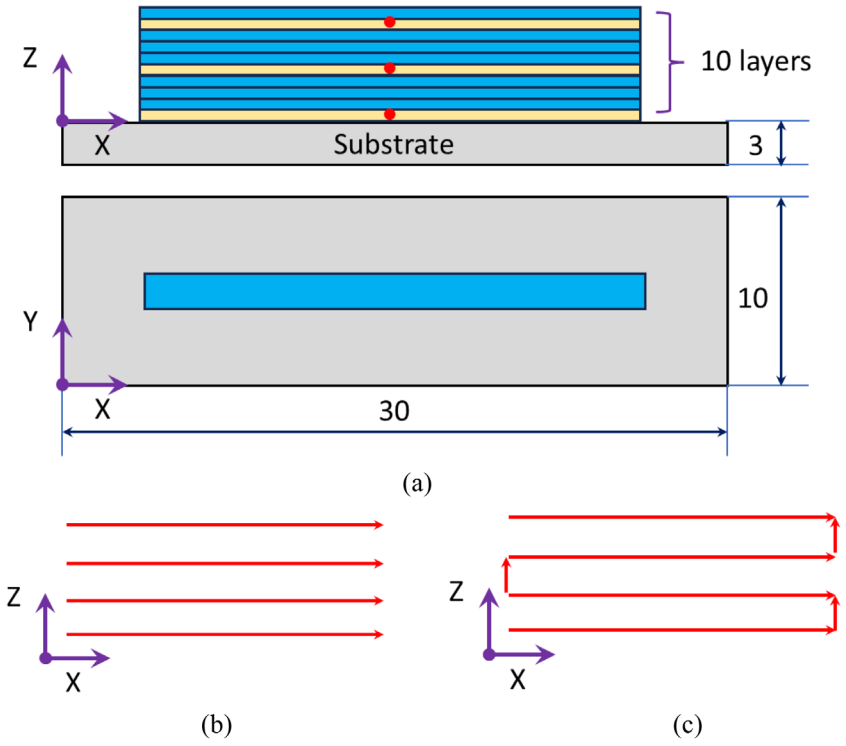

Fig. 1. (a) Schematic presentation of the model, (b) single direction of scanning (SDS), and (c) reverse direction of scanning (RDS).

2 Numerical simulation

In this article, the temperature and stress fields of Inconel 625 thin-walled parts formed by Direct Laser Metal Deposition (DLMD) were simulated in ANSYS software. The two Inconel 625 thin walls were formed on the 316L stainless steel substrates according to the single direction and the reverse direction scanning methods.

The composition of Inconel 625 powder is shown in Table 1 [10], while that of 316L stainless steel is shown in Table 2 [11]. The dimensions of the thin-walled model are shown in Figure 1a. The substrate has a size of 30 mm × 10 mm × 3 mm (length × width × thickness), and a cladding layer has a size of 20 mm × 0.5 mm × 0.1 mm (length × width × thickness). The deposited thin wall consists of 10 layers.

To reduce computational complexity, a finer regular mapped mesh was used for the cladding layer, while a coarser hexahedral mesh and tetrahedral mesh were used for the substrate and the transition between the substrate and the part, respectively, as shown in Figure 2. The mesh elements of the substrate were modeled by SOLID98 tetrahedral coupled elements with ten nodes, while the cladding layer elements were SOLID5 hexahedral coupled elements with eight nodes.

The process parameters are shown in Table 3. The initial temperature of the substrate was 20 °C, which is the ambient temperature, and the boundary condition is convective heat transfer. The latent heat treatment is assumed to vary with temperature, and the activated element pool has no convective heat transfer at the melting temperature. The stress at the beginning of the process is

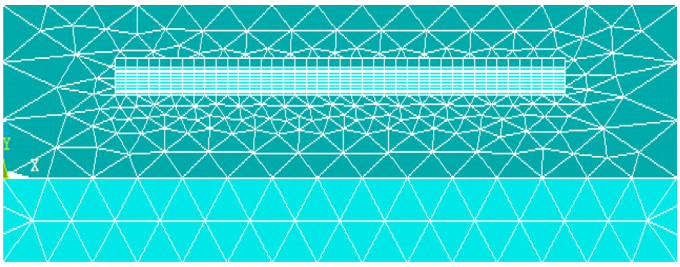

Fig. 2. The mesh model of the substrate and cladding layers.

Table 3. Process parameters.

Laser power (W)	Scanning speed (mm/s)	Powder feeding rate (g/min)	Laser diameter (mm)	Initial temperature (°C)
250	10	2.8	0.5	20

assumed to be free stress, and the reference temperature of the substrate and cladding material is the ambient temperature and the melting temperature, respectively. One element is activated every 0.05 seconds, with a heat flow area of 0.5×0.5 mm^2. Finally, different scanning methods are defined by activating the corresponding elements, as shown in Figures 1b and 1c. In the single direction scanning (SDS) method, the nozzle pauses for one second at the end of a deposited layer, and then moves back to the beginning of the next layer for the deposition (Fig. 1b). On the other hand, in the reverse direction scanning (RDS) method, at the end of a deposited layer, the nozzle pauses for one second before moving up in the Z direction, and immediately begins scanning the next layer (Fig. 1c).

As mentioned, the laser beam in the DLMD process strikes the substrate and melts the powder particles. The bead is formed continuously by moving the laser beam over the surface. The temperature field is calculated by solving the 3D heat conduction moving heat source equation shown in equation (1) [12].

$$\rho c_p \frac{\partial T}{\partial t} - \rho c_p \nabla(UT) - \nabla.(K\nabla T) = Q, \tag{1}$$

where ρ, c_p, and K are the density, heat capacity, and thermal conductivity, respectively. U is the heat source speed and Q is the heat generation that is not considered in this analysis. As mentioned with the finite element method, the moving heat source is not directly considered. However, the continuous addition of the material to the substrate is divided into many small time steps, and for each time step, a stationary heat transfer equation is solved. The APDL subroutine defines the position of the laser beam at a given time step as a function of U and the beam diameter. Therefore, equation (1) is simplified to equation (2) and should be solved for each time step with its corresponding boundary conditions.

$$\rho c_p \frac{\partial T}{\partial t} - \nabla.(K\nabla T) = Q. \tag{2}$$

The boundary conditions are:

$$-K(\nabla T.n)|_{\xi} = \begin{cases} -h(T - T_0) - \varepsilon\sigma\left(T^4 - T_0^4\right), \\ -h(T - T_0) \end{cases} \tag{3}$$

where h is the convection heat transfer, and ε and σ are the radiation coefficient and Stephen Boltzmann constant, respectively. The shielding gas effect beside the radiation from the molten pool is considered in the boundary condition of the molten pool. All sides of the substrate have a convection heat transfer boundary condition. The conditions of equation (4) should also be satisfied:

$$T(x, y, z, 0) = T(x, y, z, \infty) = T_0. \tag{4}$$

The material properties are defined to be temperature dependent, and the latent heat of fusion is considered in the definition of specific heat.

The total strain can be written as the sum of the individual components of the strain:

$$\varepsilon_{kl} = \varepsilon_{kl}^E + \varepsilon_{kl}^P + \varepsilon_{kl}^T, \tag{5}$$

where k, $l = \{1,2,3\}$, ε^E, ε^P, and ε^T are the elastic, plastic, and thermal strains, respectively. The transformation plasticity and volume dilatation strains are not considered in this model.

3 Experiment

3.1 Fabrication of samples

The DLMD forming system used in the experiments comprises a 0.5KW Fiber laser, powder feeder, powder nozzle, and a three-axis linkage workbench (Fig. 3). The Inconel 625 powder with a particle size ranging from 15 to 55 μm was used (Fig. 4), and its composition is shown in Table 1. The substrate material is 316L stainless steel, with its composition indicated in Table 2. The substrate

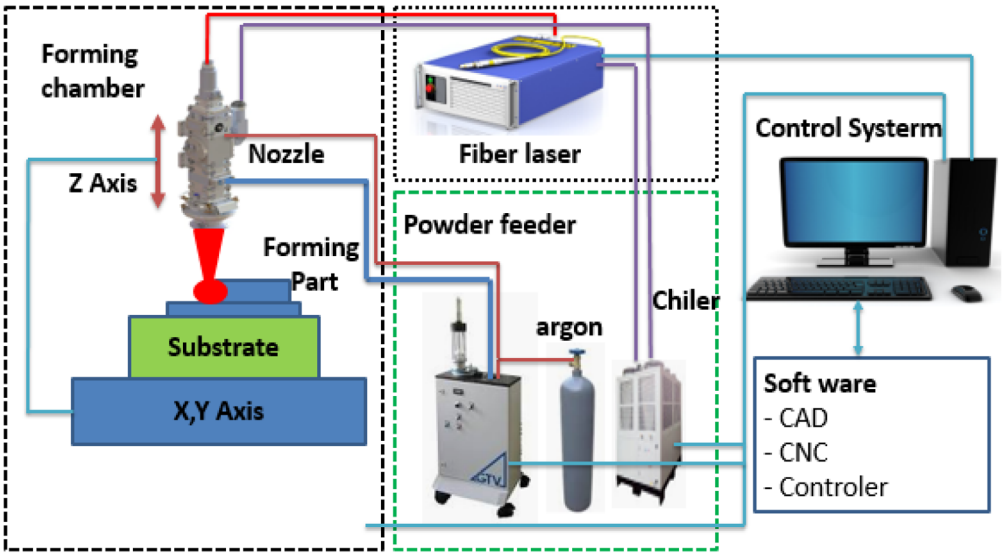

Fig. 3. The schematic of DLMD system.

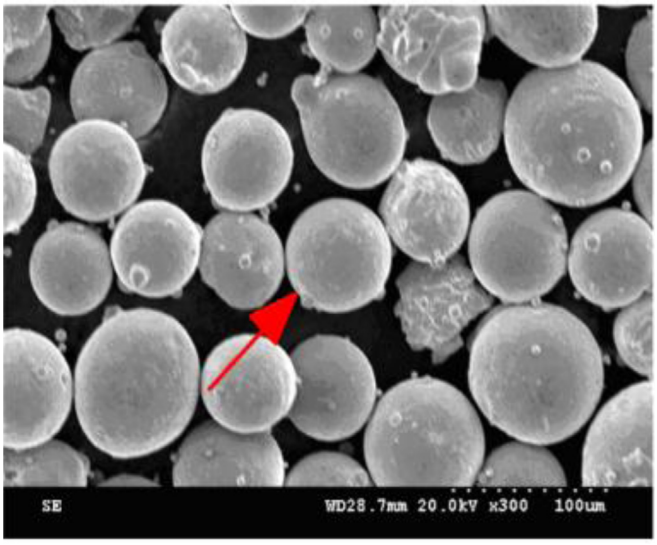

Fig. 4. SEM image of Inconel 625 powder.

dimensions are 100 mm × 50 mm × 10 mm (length × width × thickness). Prior to the experiment, the metal powder was dried in a vacuum drying oven at 200 °C for four hours to eliminate moisture. The substrate was polished with sandpaper and then cleaned with acetone and ethanol to remove grease and stains.

To investigate the effects of stress distribution on the occurrence of cracks and warping in the cladding layer, the two thin walls were built with the process parameters shown in Table 3 and the forming information presented in Table 4. In both cases, each deposited layer was programmed with a length of 40 mm and a width of 0.5 mm. The walls were built with 100 deposited layers. The average layer thickness value is about 0.1 mm, so the wall height is about 10 mm. Each layer is formed by one track. Figures 5 and 6 show the fabricated Inconel 625 thin-walled parts in the experiment.

3.2 Microstructure and microhardness tests

To observe microstructures and microhardness, the two thin wall parts have been sectioned into small samples that correspond to areas A, B, C, D, E, F as illustrated in Figures 5a, 6a, and 7a. The samples were ground, polished and etched by a solution of phenolic acid before observing the microstructure on a digital optical microscope (A2M AXIO, Carl Zeiss).

The hardness of each of these small samples is measured using a hardness tester (Duramin). Figure 7b depicts the measurement diagram where the row '1' corresponds to the bottom layer, the row '2' represents the middle area, and the row '3' depicts the top area of the thin component. Figure 7c illustrates a microhardness test result.

4 Results and discussion

4.1 Temperature simulation results

The temperature distribution and the thermal cycles after completing the tenth layer of the thin walls under two different scanning methods was shown in Figures 8 and 9, respectively. The thermal cycles plotted in Figure 9 were based on the thermal data extracted from the middle points of the first layer (L1), the fifth layer (L5), and the ninth layer (L9) of the walls in both the SDS and RDS methods, as illustrated by the red points in Figure 1a.

As depicted, the temperature gradient varies between the two scanning methods due to their unique characteristics. In the SDS method, the laser beam scans one layer, then it pauses for one second before moving to the starting point and begins to scan the next layer (Fig. 1a). This leads to a longer cooling time for the previous layer, resulting in a larger temperature gradient of the cladding layer (Fig. 8a). On the other hand, in the RDS method, the laser beam scans a layer, pauses for one second at the end of the layer before moving up in the Z direction, and then immediately begins scanning the next layer (Fig. 1c). As a result, the

Table 4. Simples and their dimensions.

Simples	Scanning methods	Dimension (mm)	Layer numbers
No. 1	Single direction of scanning	40 × 0.5 × 10	100
No. 2	Reverse direction of scanning	40 × 0.5 × 10	100

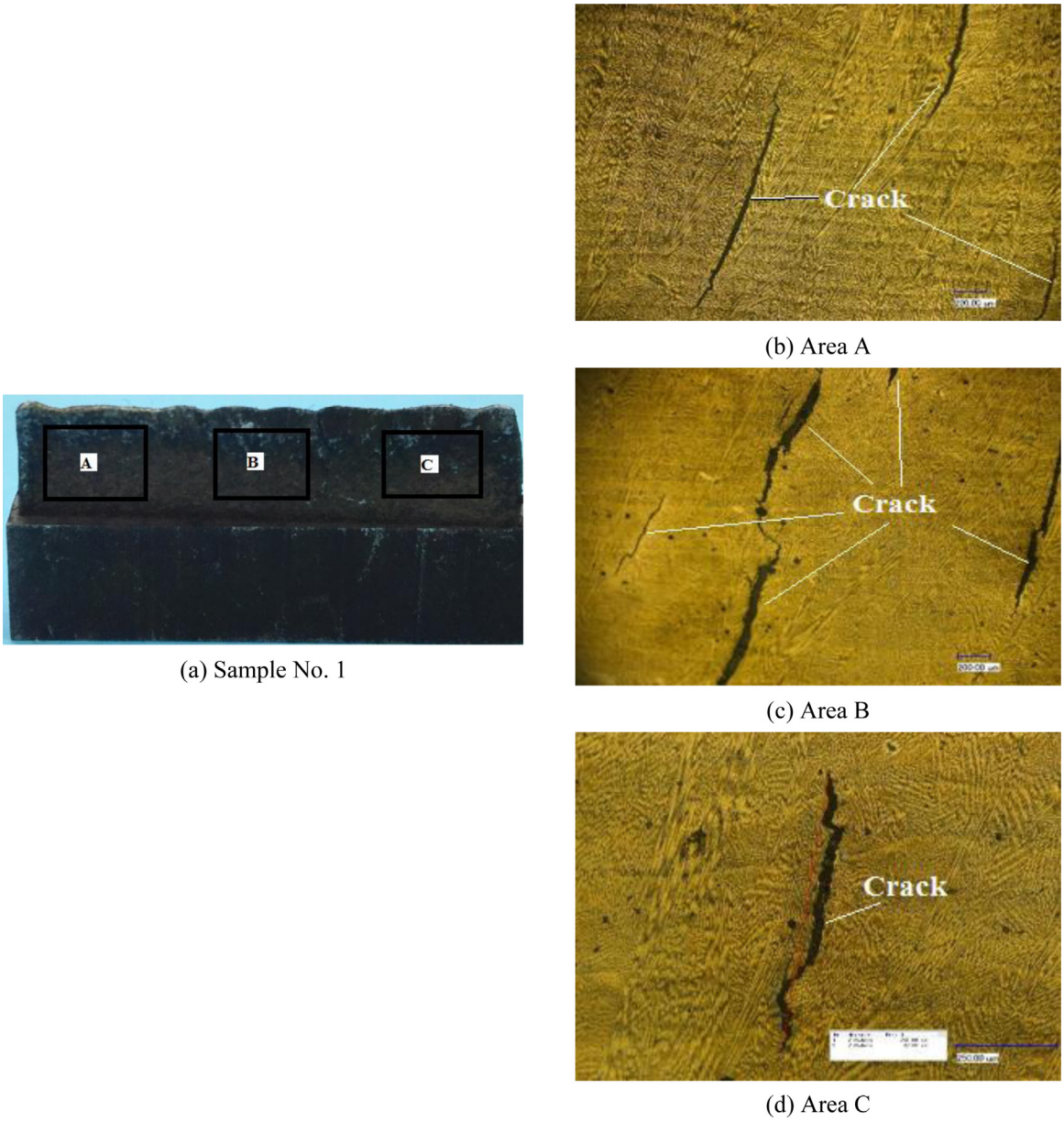

(a) Sample No. 1

(b) Area A

(c) Area B

(d) Area C

Fig. 5. (a) The fabricated sample no. 1 and the optical microstructure images in (b) the area A, (c) the area B, and (d) in the area C.

cycle time between the two successive peaks in the RDS method is shorter than in the SDS method (Fig. 9). The shorter cooling time of the previous layer results in a smaller temperature gradient (Fig. 8b).

Moreover, due to the longer cooling time in the SDS method, the interlayer temperatures in the SDS method is smaller compared to those in the RDS method (Fig. 9). For example, the interlayer temperature at the beginning of the second layer in the SDS method is about 46 °C, whereas that value in the RDS method is about 53 °C. When the number of layers increases, the interlayer temperature also increases, indicating the heat accumulation phenomenon, and the difference between the SDS and RDS methods is more significant. The interlayer temperature after the

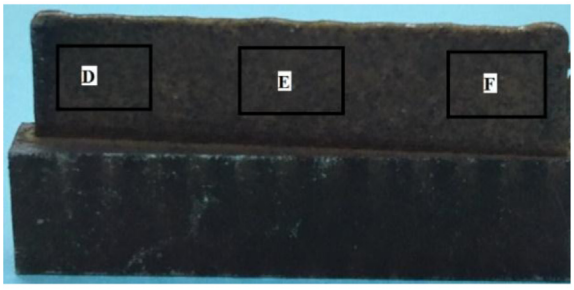

(a) Sample No. 2

(b) Area D

(c) Area E

(d) Area F

Fig. 6. (a) The fabricated sample no. 2 and the optical microstructure images in (b) the area D, (c) the area E, and (d) in the area F.

deposition of the first layer, the fifth layer, and the ninth layer in the SDS method are 46 °C, 123 °C, and 190 °C, respectively. Meanwhile, these values in the RSD method increases to 53 °C, 146 °C, and 227 °C.

Based on the thermal simulation results, we can also estimate the average cooling rate from the pick temperature to the interlayer of each deposited layer, which can be used to explain the difference of grain size in microstructures between the deposited layers of the thin wall and between the same layer of the walls in the two scanning methods. The cooling rate of the first layer, the fifth layer and the ninth layer in the SDS method are 973 °C/s, 889 °C/s, and 764 °C/s, respectively, whereas those values in the RDS method are relatively lower (namely, 942 °C/s, 852 °C/s, and 731 °C/s for the first layer, the fifth layer and the ninth layer, respectively). The findings in temperature evolution in this study is also in line with those reported in previous studies [13,14].

4.2 Stress simulation results

Figure 10 shows the distribution of stress in the X, Y, Z directions, and the Von Mises stress in the thin wall fabricated by the SDS method. Figure 10a depicts the stress distribution in the X direction (parallel to the scanning direction). The middle section of the thin-walled part experiences tensile stress, with the direction of the stress along the scanning direction (from left to right). Moreover, along the height of the cladding layer, the stress increases, and it is mainly concentrated on the left side of

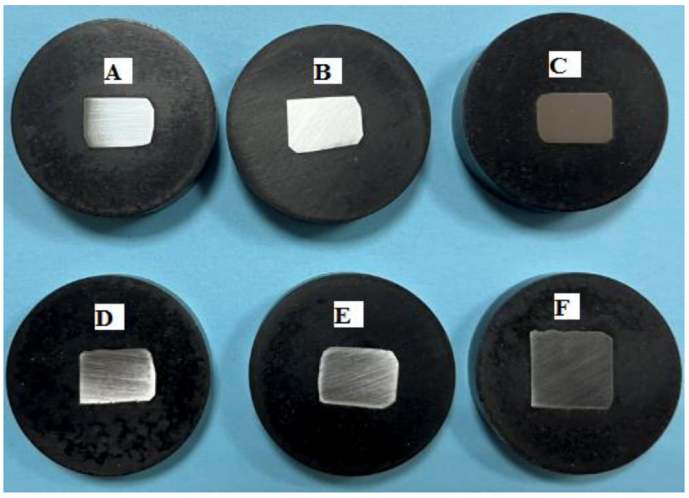

(a) Images of the cross-sections of thin walls cut from the two samples No. 1 (A, B, C) and No. 2 (D, E, F)

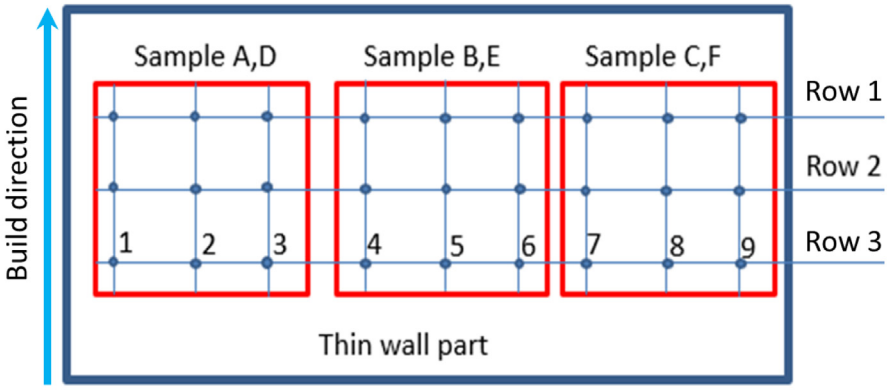

(b) Microhardness measurement positions on the cross-sections

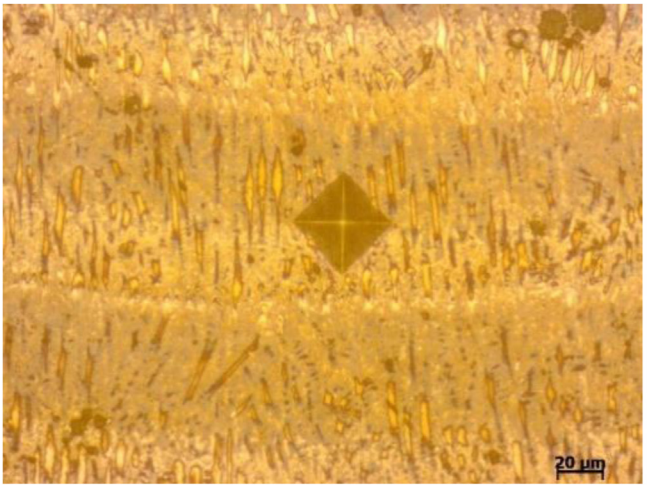

(c) An image of microhardness measurement trace

Fig. 7. Preparation of samples for microstructures and microhardness tests.

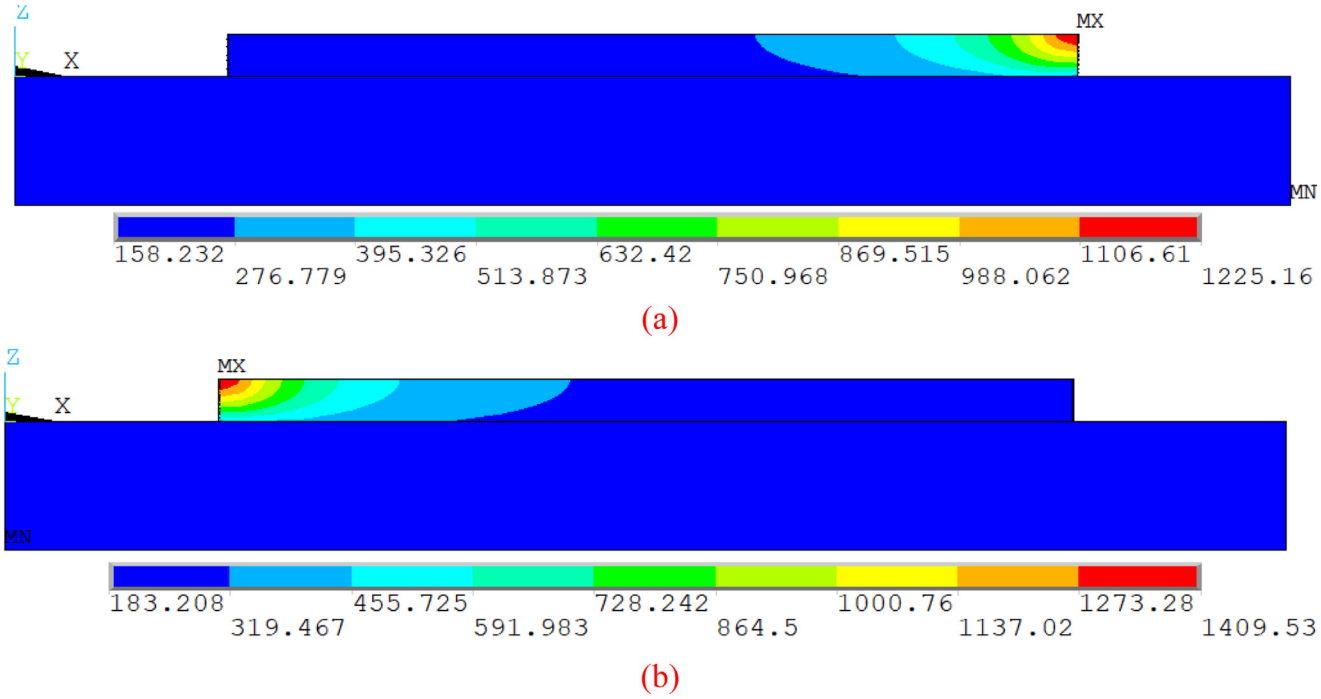

Fig. 8. Temperature distribution of the thin walls after the last deposited layer: (a) single direction of scanning (SDS) and (b) reverse direction of scanning (RDS).

the middle. Figure 10b shows the stress distribution in the Y direction (i.e., the thickness direction). The stress distribution in the middle is relatively uniform and it is tensile stress. The stress at the left end is compressive stress.

Figure 10c shows the stress distribution in the Z direction perpendicular to the scanning direction. The stress distribution in the middle is relatively uniform, and along the height of the thin-walled part, the stress tends to increase. The stress at the left end is compressive stress, while the stress at the right end is tensile stress. Generally, the stress in the X direction is greater than that in the Y and Z directions, and the total stress at the node results from the combination of stresses in all three directions. The Von Mises stress shows that the stress at both the left end and the right end of the wall is the tensile stress, while the compressive stress is present in the middle of the wall (Fig. 10d).

Figure 11 shows the stress distribution in the X, Y, Z directions, and the Von Mises stress in the thin wall deposited by the RDS method. Figure 11a shows the stress distribution in the X direction, where the stress concentration is observed in the middle with a tensile stress and a compressive stress at both the left and right ends of the wall. This is opposite to that observed in the SDS method (Fig. 10a).

Figure 11b shows a quite uniform stress distribution with stress values at both ends and the middle of the thin-walled part. Similarly, in Figure 11c, a uniform stress distribution is observed on the thin-walled part, where the stress tends to increase along the height from compressive stress to tensile stress. Generally, the stress in the X direction is dominant and higher than the stress in the Y and Z directions, indicating that the main stress is in the X direction. However, in this case, the Von Mises stress in the wall (Fig. 11c) reveals a relatively uniform distribution as compared to that in the wall fabricated by the SDS method (Fig. 10c). The Von Mises stress in the RDS method is also lower than that in the SDS method.

To quantitatively compare the stress in the walls between the SDS and RDS methods, the Von Mises stress along the length of the first layer, the fifth layer, and the ninth layer from the left to the right (the yellow layers illustrated in Fig. 1a) were extracted and compared, as shown in Figure 12. It is shown that, in all the studied cases, the Von Mise stress in the RDS method is relatively uniform and lower than that in the SDS method. Moreover, the Von Mises stress increases with the increase in layer levels. More importantly, in the case of the SDS method, the Von Mises tress values in both the left and right ends of the wall are much higher than those in the middle area, and the tress values on the left are also higher than those in the right. The higher stress values in the SDS method compared to those in the RDS method can be explained by the higher cooling rates, as observed previously. With the longer cooling time in the SDS method, the lower interlayer temperature generated, leading to higher cooling rates during the deposition process of the wall according to the SDS method.

In conclusion, it is demonstrated that with the SDS method, the residual stress at both ends of the thin-walled part was high, while the stress at the middle is much smaller, with a stress difference between the maximum and minimum of about 1800 MPa (Von Mises stress).

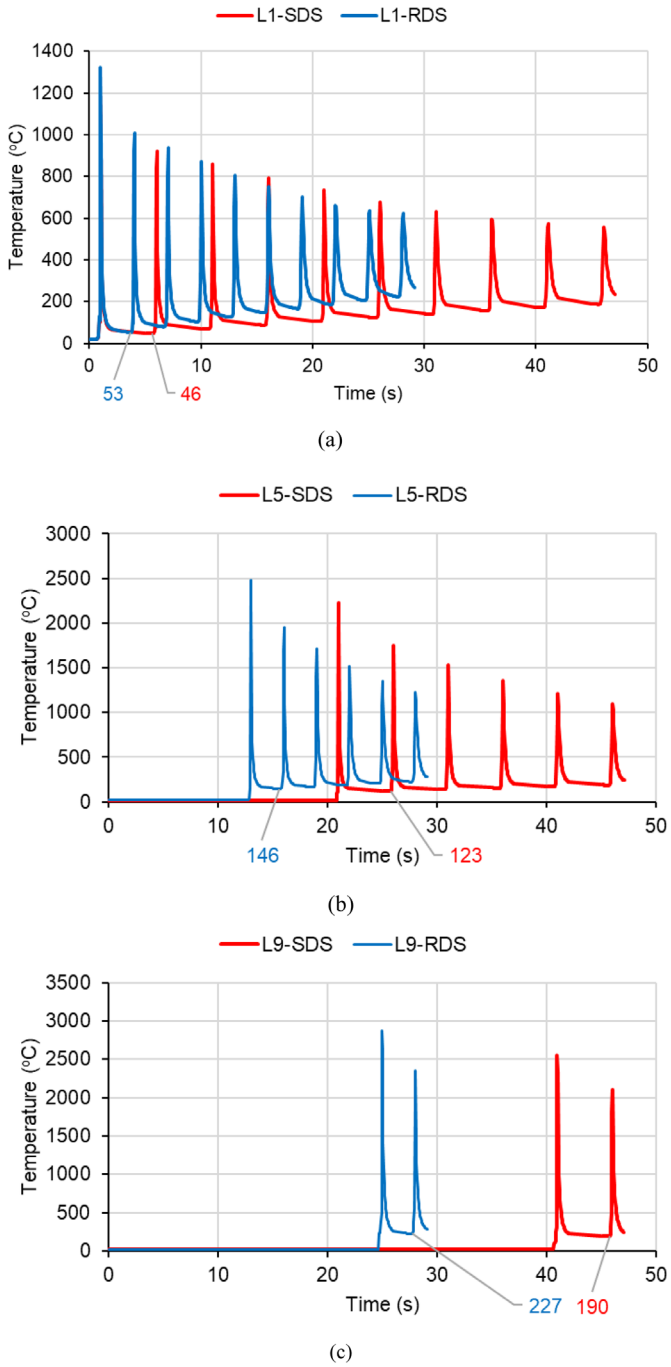

Fig. 9. The comparison of the thermal cycles between the scanning methods (SDS and RDS) at the center point of (a) the first layer (L1), (b) the fifth layer (L5), and (c) the ninth layer (L9).

In contrast, with the RSD method, the residual stress in the thin-walled part was distributed relatively evenly, with a stress difference of about 350 MPa (Von Mises stress) between both ends and the center. As a result, it can be considered that the RDS method is better in terms of balancing the residual stress deviation in the built wall.

4.3 Crack formation

Figure 5 presents the wall fabricated by the SDS method. It is revealed that there are greater number and size of cracks in the middle layers as compared to those at the two ends of the wall. On the other hand, the second wall formed by the RDS method had no cracks at the end regions and in the middle region (Fig. 6). Indeed, in the wall fabricated by the SDS method, high tensile stress occurs in the end regions (Fig. 10c), and there is a large stress deviation between the ends and the middle region of the wall (Fig. 12). As a result, cracks will appear when the stress exceeds the tensile strength of the material. Conversely, under the RDS method, the stress deviation is lower, so no cracks appear during the forming process of the thin-walled part.

Figure 13 displays SEM images of a crack. Figure 13a shows a close-up of the crack, and Figure 13b provides a detailed view of the crack mouth. Notably, Figure 13b reveals bright areas on the oxidized crystal and columnar structures on the surface of the crystal, with a liquid layer coating the top. This indicates that the crack formed due to high-temperature conditions, and the crystal boundaries were separated by liquid layers. Thus, the observed crack is a typical sample of a hot crack.

DLMD is a technology that utilizes a unique process where the shaping material is rapidly heated to a molten state, followed by a fast-cooling process during crystallization. When subjected to a high-energy laser beam, the metal area and its surroundings reach an extremely high temperature and partially melt, causing the affected material area to expand and undergo compressive stress, which is constrained by neighboring areas. This results in a decrease in stress value as the temperature increases. However, the stress value at the center of the molten area may exceed the allowable limit, leading to plastic deformation under elastic deformation.

During the crystallization process, the constrained molten area is subjected to tensile stress as it is not free to shrink and must be confined by surrounding areas. The extremely fast cooling rate causes an uneven distribution of chemical components, resulting in high-melting-point elemental clusters crystallizing before low-melting-point ones. This leads to liquid membranes separating from the crystal cluster boundary, which creates cracks. Due to the columnar crystal structure of the DLMD material (as shown in Fig. 5), cracks tend to develop along the boundary between crystal clusters.

In summary, the DLMD shaping technology rapidly heats and cools the shaping material, causing compressive and tensile stresses. Uneven distribution of chemical components during crystallization leads to crack formation. The columnar crystal structure of DLMD material causes cracks to develop along crystal cluster boundaries.

4.4 Microstructure analysis

An important characteristic of Inconel 625 alloy material fabricated by the DLMD technology is the presence of very small, long, vertically developed columnar crystal structures, as illustrated in Figure 14. This is due to the

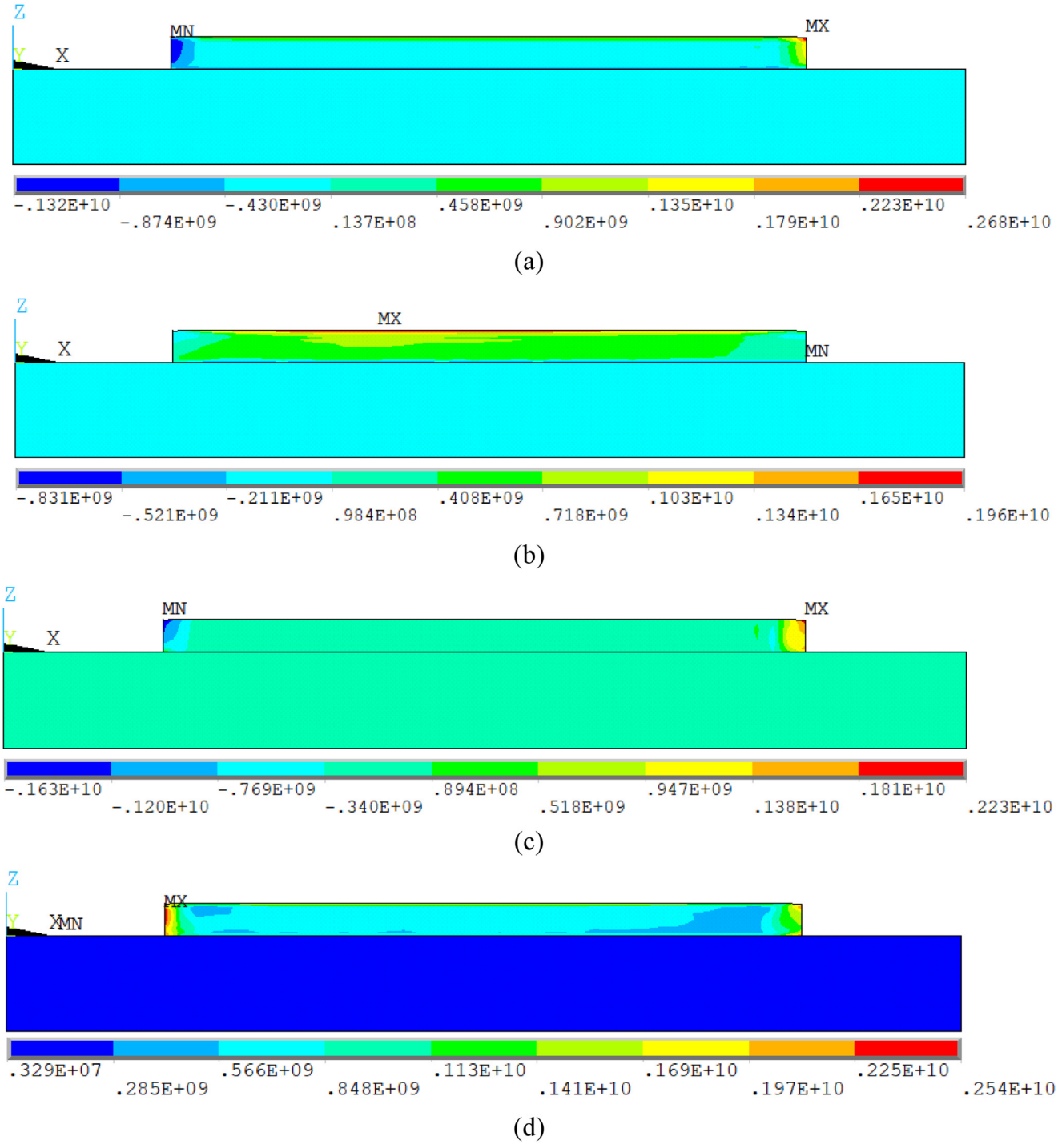

Fig. 10. Stress distribution in the wall fabricated by the SDS method: (a) X stress distribution, (b) Y stress distribution, (c) Z stress distribution, and (d) Von Mises stress distribution (unit in Pa).

rapid crystallization rate and large temperature gradient, resulting in small and uniform crystal structures. The crystallization process occurs at the boundary surface between the solid and liquid phases, ensuring that the liquid and solid phases remain in contact throughout the entire process. This type of crystal structure is typical of columnar crystals. Figure 14a also depicts the continuous bonding between the deposited layers, which not only enhances the mechanical properties, but also ensures the continuous development of crystal structures between the layers.

Figure 14a illustrates the microstructure of the walls shaped by the SDS method. The microstructure of the two basic samples is quite similar, featuring columnar structures. The wall shaped using the SDS method exhibits a continuously developed columnar crystal structure

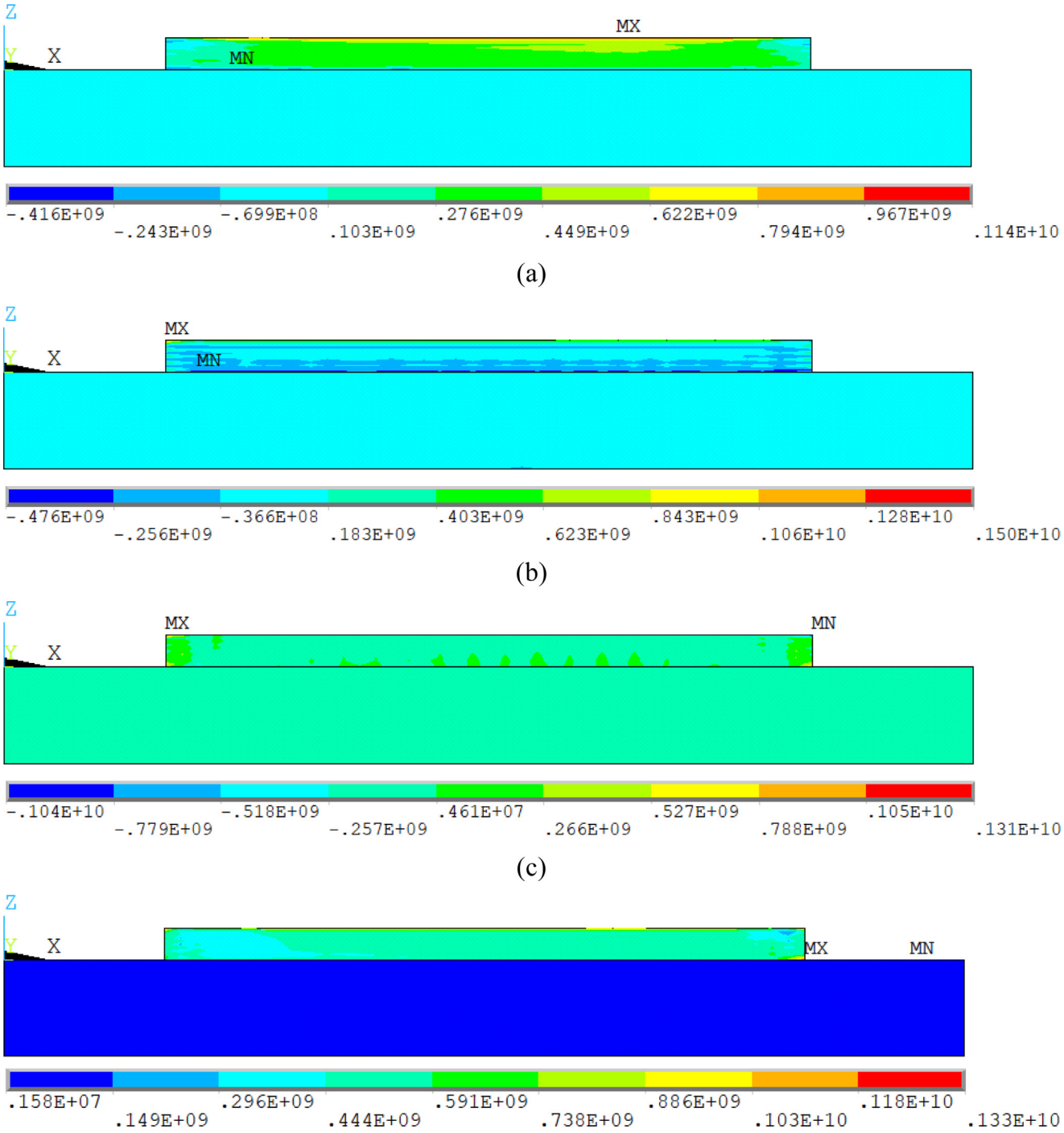

Fig. 11. Stress distribution in the wall fabricated by the RDS method: (a) X stress distribution, (b) Y stress distribution, (c) Z stress distribution, and (d) Von Mises stress distribution *(unit in Pa)*.

between the shaped layers, with long crystal lengths and vertical development along the height of the shaped layers, shown in Figure 14a.

The wall shaped by the RDS method also has a columnar crystal structure, but the development direction is oblique, with shorter crystal lengths and no continuous development between the shaped layers, shown in Figure 14b.

According to the rapid solidification theory, the microstructural dimension depends on the cooling speed. The cooling rate V can be expressed by equation (6) [15]:

$$V = G \times R, \tag{6}$$

where the G is the temperature gradient and R is the solidification rate. Regarding the SDS method, the beginning scanning time for the second layer is longer

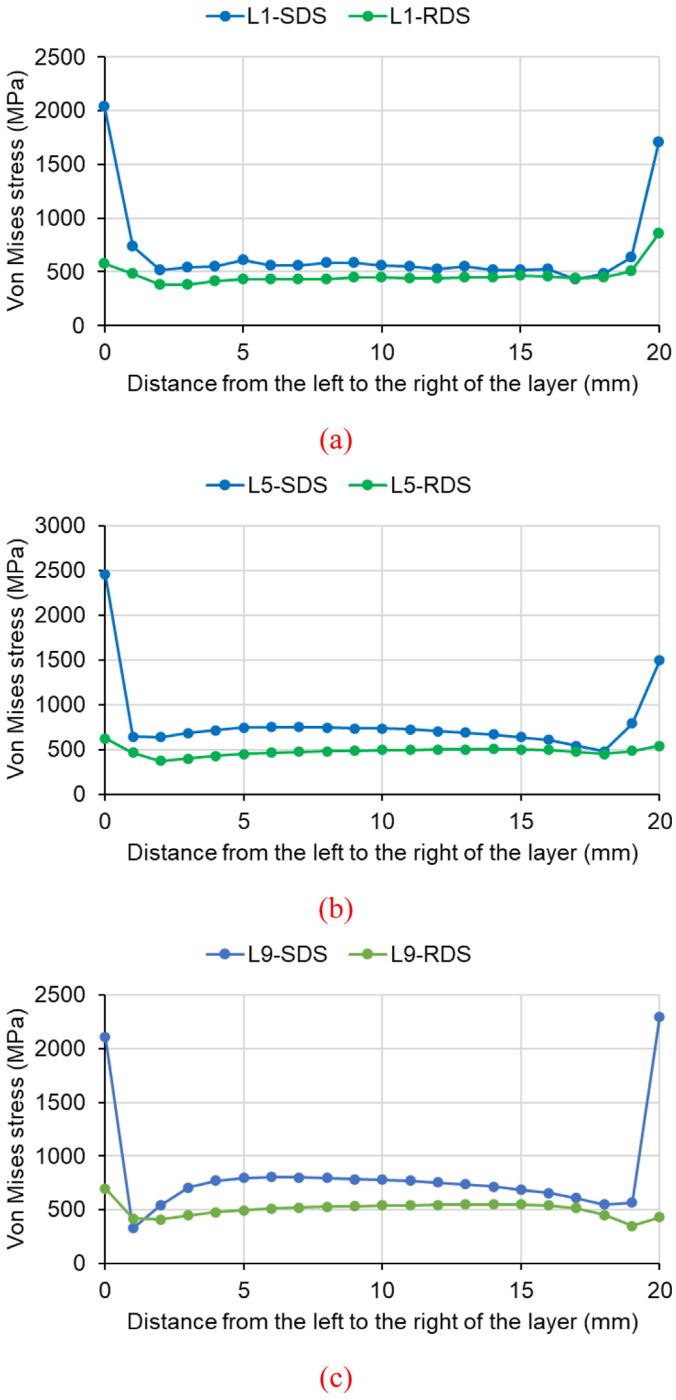

Fig. 12. Comparison of the Von Mises stress in the walls between the SDS and RDS methods: (a) along the first layer, (b) along the fifth layer, and (c) along the ninth layer.

because the nozzle needs to return to its initial position, leading to a significant reduction in the interlayer temperature and larger temperature gradient between the two layers. Consequently, the cooling rate V is higher compared to that in the RDS method, as analyzed in

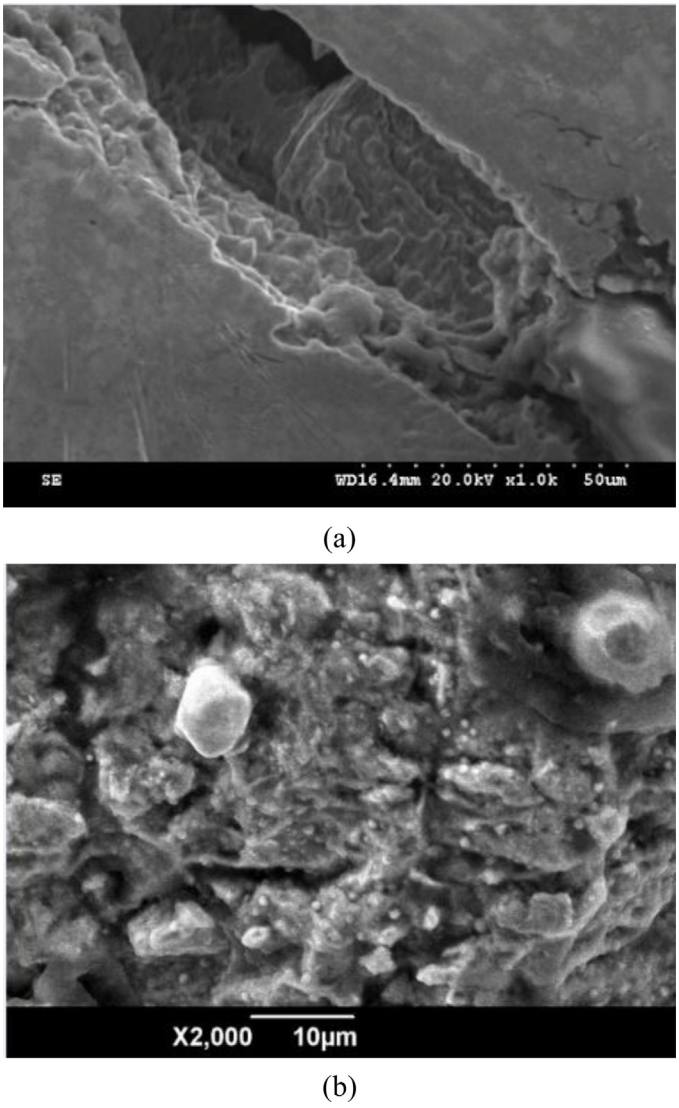

Fig. 13. SEM images of cracks on the component: (a) the crack morphology and (b) the crack mouth.

Section 4.1, and heat transfer occurs from the top layer to the bottom layer, resulting in the formation of very thin cylindrical-crystal structures in the vertical direction.

In contrast, in the RDS method, the cooling time is short. As a result, the temperature gradient between the two layers is smaller, and the cooling rate V is lower, as discussed in Section 4.1. Heat transfer occurs to both sides of the wall, leading to the development of obliquely oriented cylindrical crystal structures.

Figure 15 shows the cross-section of columnar crystal structures in microstructures within a layer. It is revealed that the microstructures features relatively uniform grains with a size of around 5–7 μm. The cross-section size of columnar crystal structures in the SDS sample is relatively smaller than that in the RDS sample. The average grain size of the SDS sample is 3.70 ± 0.51 μm, while the average

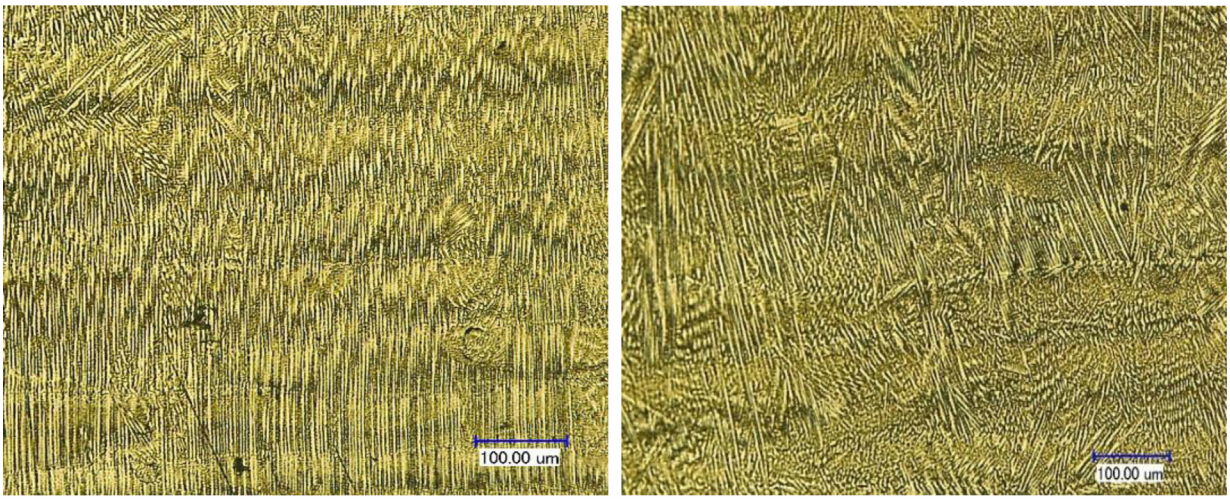

Fig. 14. Microstructure images in the cross-section along the vertical plane and scanning direction: (a) the SDS sample and (b) the RDS sample.

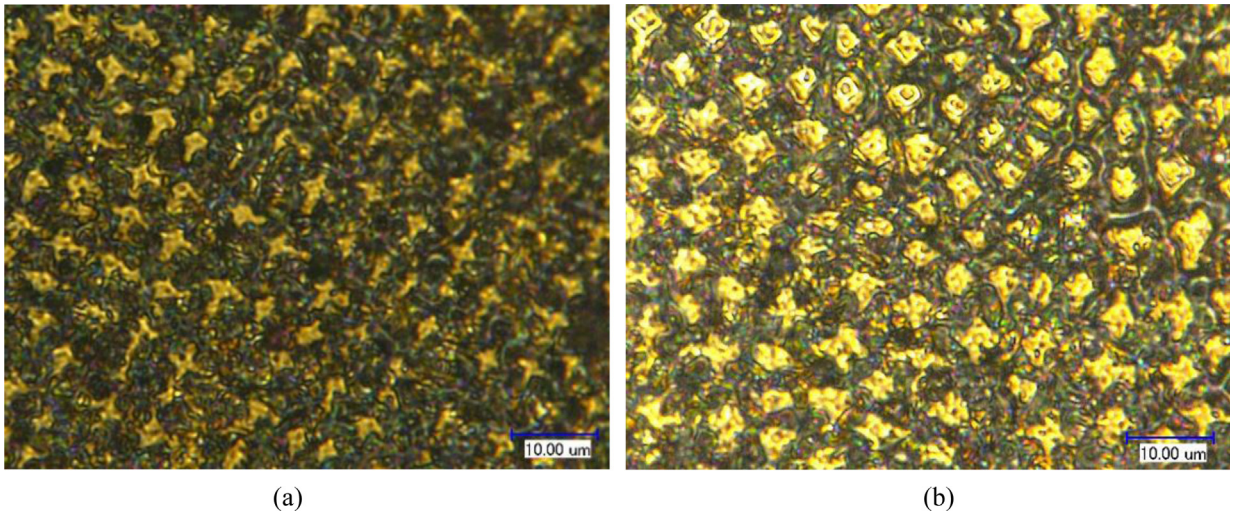

Fig. 15. Microstructural image in the horizontal plane and perpendicular to the build direction: (a) the SDS sample and (b) the RDS sample.

grain size of the SDS sample is 4.80 ± 0.66 μm. As discussed above, the cooling rate in the SDS sample is higher than that in the RDS sample. However, the difference in the grain size of microstructures is insignificant.

4.5 Microhardness analysis

Figure 16a shows the microhardness measurement values at positions on samples A, B, and C of thin wall no. 1, corresponding to the part formed by the SDS method. Figure 16b shows the microhardness measurement values at positions on samples D, E, and F of thin wall no. 2, corresponding to the part formed by the RDS method. The results indicate that, in both cases, the microhardness increases with the height of the formed layers. The microhardness values in the left, right, and middle areas are relatively uniform. In the thin wall no. 1, the microhardness measurement values range from 420 HV to 435 HV. In the thin wall no. 2, the microhardness measurement values range from 420 HV to 450 HV. These results in microhardness are in line with the observation in microstructures. Indeed, the crystal structures is formed and developed vertically with the increase in width size along the build direction. As a result, the microhardness decreases from the bottom to the higher layer of the wall.

Moreover, during the deposition process, the heat accumulation causes the temperature of the molten pool in the upper layers to gradually increase. This leads to the overflow of molten material to both sides, reducing the height of the shaping layer and increasing material density. Consequently, microhardness also gradually increases. Once the height of the shaping layer reaches a certain value and heat accumulation stabilizes, the temperature of the molten pool stops increasing. This stabilizes the

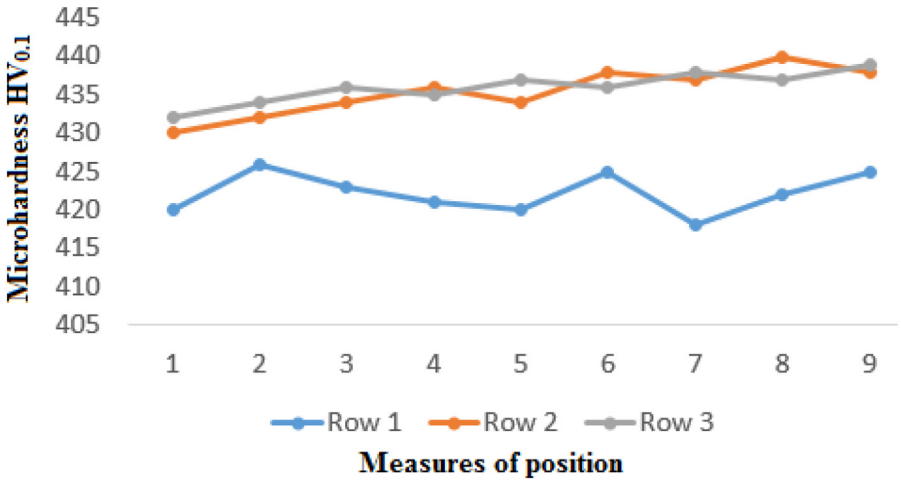

(a) The microhardness measurements result were performed on the samples A, B, and C

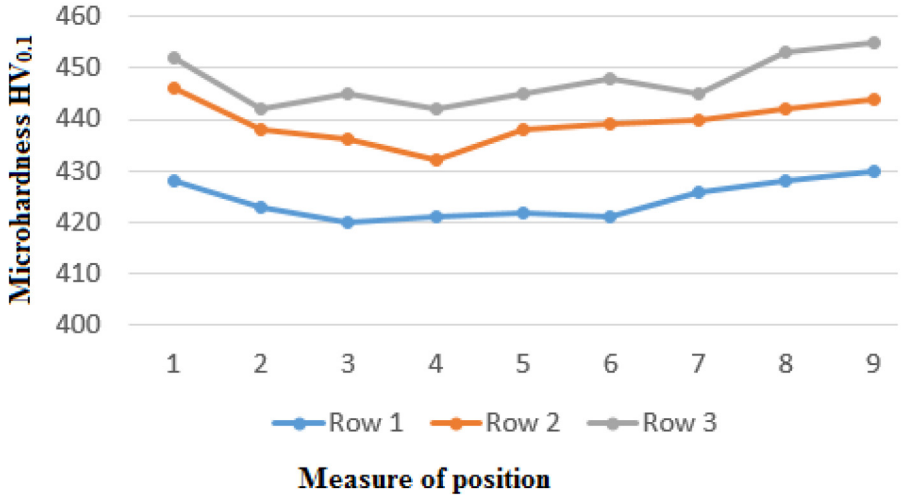

(b) The microhardness measurements result were performed on the samples D, E, and F.

Fig. 16. Microhardness measurement results of the thin walls no. 1 and no. 2.

thickness of each layer and results in the microhardness reaching a stable state with no further increase. Although there are differences in the distribution of microhardness in both cases, the changes are not significant. This can be explained by the insignificant difference in the grain size between the SDS and RDS samples. Herein, the average grain size of the SDS sample is 3.70 ± 0.51 μm compared to 4.80 ± 0.66 μm of the RDS sample.

5 Conclusion

During the DLMD process of thin-walled parts, the scanning method used significantly affects the magnitude and distribution of residual stresses within the parts. The single direction scanning (SDS) method results in higher and unevenly distributed residual stresses, with a difference of up to 1800 MPa (Von Mises stress) between the ends and in the middle region of the wall. On the other hand, reverse direction scanning (RDS) method leads to smaller and more evenly distributed residual stresses, with a difference of around 350 MPa (Von Mises stress) between the ends and in the middle region of the wall.

Under the SDS method, cracks are often observed in the middle of the thin-walled parts, with severe cracking at both ends. The direction of cracking is generally perpendicular to the main stress direction. In contrast, under the RDS method, no cracks are typically observed within the thin-walled parts and no cracking occurs at either end.

The microstructure of the Inconel 625 material in the forming layer is characterized by a columnar crystal structure that has a small length and grows perpendicularly to the scanning direction. This growth is continuous between the forming layers.

In both cases, the microhardness increases with the height of the formed layers; the microhardness values in the left, right, and middle regions are relatively uniform, the microhardness measurement values range from 420 HV to 450 HV.

Funding

This research is funded by Vietnam National Foundation for Science and Technology Development under grant number KC4.0-15/19-25.

Conflict of Interest

The authors declare that they have no competing interests.

Data availability

All data generated and analyzed during this study are included in this article.

Authors contributions

Tat Khoa Doan and Van Thao Le are involved in the conceptualization and methodology; Tat Khoa Doan, Van Thao Le, Van Chau Tran, and Van Nguy Duong contributed to the formal analysis and investigation; Tat Khoa Doan, Van Thao Le, and Van Nguy Duong contributed to writing—original draft preparation; all the authors contributed to writing, review, and editing; Tat Khoa Doan acquired the funding.

References

1. G. Jie, M. Qingchao, S. Yan, W. Kangning, S. Qiang, W. Canming, Effect of Nb content on microstructure and corrosion resistance of Inconel 625 coating formed by laser cladding, Surf. Coat. Technol. **458** (2023) 12931
2. A. Grabos, P. Rutkowski, J. Huebner, P. Nieroda, D. Kata, S. Hayashi, Thermal properties of Inconel 625-NbC metal matrix composites (MMC), Mater. De. **224** (2022) 111399
3. F. Chena, Q. Wang, C. Zhang, Z. Huang, M. Jia, Q. Zhang, Mcrostructures and mechanical behaviors of additive manufactured Inconel 625 alloys via selective laser melting and laser engineered net shaping, J. Alloys Compd. **917** (2022) 165572
4. D. Ren, Z. Xue, Y. Jiang, X. Hu, Y. Zhang, Influence of single tensile overload on fatigue crack propagation behavior of the selective laser melting Inconel 625 superalloy, Eng. Fract. Mech. **239** (2020) 107305
5. L. Zhou, S. Chen, C. Zhang, J. Liang, T. Cui, C. Liu, M. Wang, Microstructure evolution and properties of direct laser deposited 24CrNiMoY alloy steel assisted by non-contact ultrasonic treatment, Mater. Sci. Eng. A **811** (2021) 141088
6. N. Shamsaei, A. Yadollahi, L. Bian, S.M. Thompson, An overview of direct laser deposition for additive manufacturing; Part II: mechanical behavior, process parameter optimization and control, Additive Manuf. **8** (2015) 12–35
7. Z.U. Arif, M.Y. Khalid, E. Rehman, Laser-aided additive manufacturing of high entropy alloys: processes, properties, and emerging applications, J. Manuf. Processes **78** (2022) 131−171
8. Z. Lin, C. Suiyuan et al., Microstructure and properties of 24CrNiMoY alloy steel prepared by direct laser deposited under different preheating temperatures, Mater. Character. **158** (2019) 109931
9. L. Shihua, C. Bo, T. Caiwang, S. Xiaoguo, Effects of oxygen content on microstructure and mechanical properties of 18Ni300 maraging steel manufactured by laser directed energy deposition, Opt. Laser Technol. **153** (2022) 108281
10. J. Wang, W. Yachao, S. Yutai, J. Shi, Evaluation of in-situ alloyed Inconel 625 from elemental powders by laser directed energy deposition, Mater. Sci. Eng. **830** (2022) 142296
11. Z. Songtao, B. Fengqin, W. Tao et al., Microstructural investigation of the effect of hot-isostatic-pressing treatment on a laser powder bed fused type 316L stainless steel, Mater. Character. **197** (2023) 112716
12. E. Foroozmehr, R Kovacevic, Effect of path planning on the laser powder deposition process: thermal and structural evaluation, Int. J. Adv. Manuf. Technol. **51** (2010) 659–669
13. R. Li, G. Wang, X. Zhao et al., Effect of path strategy on residual stress and distortion in laser and cold metal transfer hybrid additive manufacturing, Additive Manuf. **46** (2021) 102203
14. J. Huang, Z. Guan, S. Yu et al., A 3D dynamic analysis of different depositing processes used in wire arcadditive manufacturing, Mater. Today Commun. **24** (2020) 101255
15. Y. Huang, X. Zeng, Investigation on cracking behavior of Ni-based coating by laser-induction hybrid cladding, Appl. Surf. Sci. **256** (2010) 5985−5992

Cite this article as: Tat Doan Khoa, Van Thao Le, Van Nguy Duong, Van Chau Tran, Effects of scanning methods on cracking, microstructures and microhardness of Inconel 625 parts formed by direct laser metal deposition, Manufacturing Rev. 11, 2 (2024)